Secondary Frequency Control Considering Optimized Power Support From Virtual Power Plant Containing Aluminum Smelter Loads Through VSC-HVDC Link

Peng Bao, Wen Zhang, and Yuxi Zhang

***Abstract*—The growing number of renewable energy replacing conventional generators results in a loss of the reserve for frequency control in power systems, while many industrial power grids often have excess energy supply due to abundant wind and solar energy resources. This paper proposes a secondary frequency control (SFC) strategy that allows industrial power grids to provide emergency high-voltage direct current (HVDC) power support (EDCPS) for emergency to a system requiring power support through a voltage source converter (VSC) HVDC link. An architecture including multiple model predictive control (MPC) controllers with periodic communication is designed to simultaneously obtain optimized EDCPS capacity and minimize adverse effects on the providing power support (PPS) system. Moreover, a model of a virtual power plant (VPP) containing aluminum smelter loads (ASLs) and a high penetration of wind power is established for the PPS system. The flexibility and controllability of the VPP are improved by the demand response of the ASLs. The uncertainty associated with wind power is considered by chance constraints. The effectiveness of the proposed strategy is verified by simulation results using the data of an actual industrial power grid in Inner Mongolia, China. The DC voltage of the VSCs and the DC in the potlines of the ASLs are also investigated in the simulation.**

***Index Terms*—Secondary frequency control, power support, voltage source converter (VSC), high-voltage direct current (HVDC), model predictive control (MPC), virtual power plant (VPP), demand response.**

I. Introduction

In recent years, the growing number of renewable energy sources replacing conventional power plants has become a noticeable issue [1]. The increasing concerns involve the loss of reserve for frequency control and the reduction in regulation capacity in power systems as conventional power plants are displaced. As a result, the ability of power system to counteract disturbances decreases, especially in load centers without sufficient regulation resources [2], [3]. Besides, there are many industrial power grids with sufficient energy supplies and abundant regulation resources [4]. A typical industrial power grid usually consists of self-owned generators, renewable energy sources, energy-intensive industrial loads, and some normal loads [5], [6]. Renewable energy sources can provide adequate or even surplus energy supplies, and self-owned generators have the same regulation capacity as the conventional units in power systems. Moreover, some industrial loads can be ideal flexible loads owing to their high controllability and energy-intensive characteristics [7]. If the industrial power grid could be included in the interconnected power system, it would have great potential to provide power support to the load centers lacking regulation capacity.

A viable option to connect a load center and the industrial power grid is using voltage source converter (VSC) based high-voltage direct current (HVDC) interconnections, which can flexibly provide fast emergency HVDC power support (EDCPS) for an interconnected AC power system because of its high controllability [8] - [10]. The fast and accurate EDCPS can serve as the reserve for frequency control to counteract disturbances in the system requiring power support (RPS) system, which has the same function as conventional power plants.

The applications of a VSC-HVDC system to provide EDCPS have been investigated in many research works, in which the control strategies of EDCPS can be mainly divided into two categories: additional local control strategies and coordinated control strategies. The characteristics of the two control strategies are analyzed in [11]. Additional local control usually adopts proportional control [12], [13], derivative control [14], [15], inertia emulation control [16], or a virtual synchronous generator (VSG) method [17] - [19]. As mentioned in [11], proportional-only droop control is easy to implement, but its performance is often inferior to control methods with an integral part. In [12], two droop control schemes (U_{dc}-f and P-f) are compared, where the P-f scheme adopts proportional-integral (PI) control, and the U_{dc}-f

Manuscript received: February 22, 2021; revised: April 28, 2021, accepted: August 23, 2021. Date of CrossCheck: August 23, 2021. Date of online publication: August 1, 2022.

This work was supported by the National Natural Science Foundation of China (No. 52077125) and the Science and Technology Program of the State Grid Shandong Electric Power Company (No. 2020A-126).

P. Bao, W. Zhang (corresponding author), and Y. Zhang are with the Key Laboratory of Power System Intelligent Dispatch and Control of the Ministry of Education, Shandong University, Jinan 250061, China (e-mail: 825917398@qq.com; zhangwen@sdu.edu.cn; yyuxi@foxmai.com).

DOI: 10.35833/MPCE.2021.000072

scheme adopts proportional-only droop control. Results show that the *P-f* scheme has better performance than the U_{dc}-*f* scheme. Reference [13] investigates an industrial load supplied by a VSC-HVDC link, where PI control effectively improves the power quality supplied to industrial plants. However, the role of derivative control is not considered in these references. Reference [14] adopts synthetic inertia control, where the control signal of a derivative controller is calculated according to the derivative of the frequency, i.e., the rate of change of the frequency (ROCOF). In [15], synthetic control is divided into two types: continuous control and one-shot control. The advantage of continuous control is its high adaptiveness. However, it has higher requirements for filtering. In contrast, one-shot control is simple to implement but has low adaptiveness. In [16], a novel scheme combining inertia emulation control and synthetic inertia control is proposed, which aims to blend the energy stored in the HVDC link with the power control capabilities of wind turbines. This ensures a fast frequency response with lower requirements for capacitance volume and wind turbine performance. The VSG is emerging as an alternative approach for controlling the VSCs operating in the power system. In [19], the idea of operating an inverter to mimic a synchronous generator is proposed, where an inverter operating in this way is defined as a synchronverter. According to the literature, the main difference between the synchronverter and the VSG is that the synchronverter lacks short-term energy storage. The advantages of additional local control are lower control complexity and shorter communication delays, which ensure a fast response. However, the disadvantages are also obvious. The lack of supervision and communication might cause disproportional power support, leading to undesired frequency oscillation in the providing power support (PPS) system [20].

Coordinated control usually adopts a distributed control architecture. A coordinated strategy is presented in [21], which allows all generators in different networks connected by an HVDC link to respond to frequency deviations in the RPS system without a centralized controller. The use of two droop operating modes is described in [22] and ensures the optimal operation of multiple terminals based on network characteristics. Note that these research works assume that there is no communication delay. However, [23] shows that the communication delay can obviously worsen the control performance.

From the review above, there are some gaps in the existing research. Firstly, most research works focus on EDCPS for primary frequency control (PFC), but few have studied EDCPS during the secondary frequency control (SFC) period. The short timescale of PFC leads to a contradiction: additional local control is imprecise, but the delay of coordinated control is nonnegligible. Secondly, the differences in the characteristics of the PPS system and RPS system are often not highlighted in the literature. In fact, the participation from demand side can greatly improve the flexibility of the PPS system. Thirdly, less consideration is given to the adverse effects on the PPS system caused by EDCPS such as undesired frequency oscillation and poor frequency quality.

To address the gaps, three contributions are made.

1) An model predictive control (MPC)-based SFC strategy with EDCPS is proposed. MPC controllers are included in the PPS system and RPS system to implement precise coordinated control. The communication delays are negligible for longer SFC periods.

2) An actual industrial power grid in Inner Mongolia containing self-owned generators, wind farms, and aluminum smelter loads is selected as the PPS system. In the PPS system, a model of a virtual power plant (VPP) is built to obtain high controllability.

3) The adverse effects of EDCPS on the PPS system are reduced by predictive control. The power imbalance caused by EDCPS can be counteracted in advance according to a feed-forward signal. Meanwhile, the adverse effects caused by the uncertainty associated with wind power are reduced by a chance-constraint method.

II. Framework of Proposed Control Strategy

The framework of the proposed SFC strategy is shown in Fig. 1. The two-terminal HVDC power system consists of an RPS system and a PPS system connected by a VSC-HVDC link. The RPS system consists of automatic generation control (AGC) for conventional power plants, non-AGC units and normal loads which are based on a regional load center with an insufficient reserve for frequency control. The PPS system consists of self-owned generators, wind farms, aluminum smelter loads (ASLs), and normal loads which are based on an actual industrial power grid in Inner Mongolia, China [24]. The components in the industrial power grid are integrated as a VPP model. In Fig. 1, $P_{s,1}$ and $P_{s,2}$ are the power injections of VSCs; P_{dc} is the DC power transmitted by the HVDC network; x_1 and x_2 are the state variables of RPS and PPS systems, respectively; ACE_1 and ACE_2 are the area control errors (ACEs); and $P^{G}_{set,i}$, P^{asl}_{set}, and P^{hvdc}_{set} are the set points of generator power output, ASL power consumption, and HVDC transmission power, respectively.

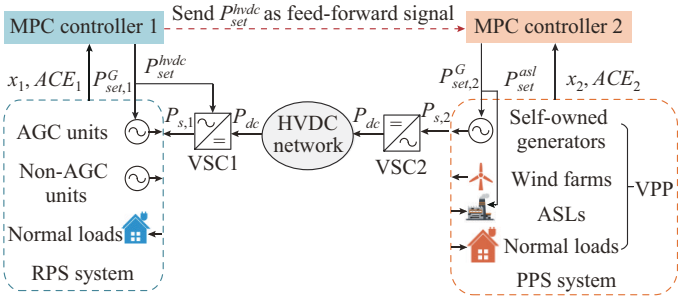

Fig. 1. Framework of proposed SFC strategy.

A distributed control architecture is adopted to provide supervision and necessary communication. There are two independent MPC controllers in the interconnected power system. The objective of the two controllers is to minimize ACE_1 and ACE_2. In each power system, MPC controller 1 or MPC controller 2 calculates the optimal control commands according to x_1 or x_2 and ACE_1 or ACE_2. To distinguish the severity of disturbances, the threshold of power support is defined as ACE_{trig}. If ACE_1 is detected to exceed ACE_{trig}, the RPS system will be considered suffering heavy disturbances. The AGC units are involved in regulation. An increment will

be added to the rated HVDC power to provide EDCPS. Meanwhile, the VPP in the PPS system will change the power output of the self-owned generators and the power consumption of the ASLs according to the received feed-forward signal to minimize the power imbalance in the PPS system. Otherwise $ACE_1 < ACE_{trig}$, EDCPS will not be triggered, and the HVDC power set point remains the rated power.

III. Model Formulation

A. SFC Model

The SFC model for the two-terminal HVDC system is shown in Fig. 2, where $P_{m,1}$ is the total mechanical output of AGC and non-AGC units in RPS system; $P_{m,2}$ is the mechanical output of self-owned generator in PPS system; $P_{nl,1}$ and $P_{nl,2}$ are the normal load consumptions in RPS and PPS systems, respectively; P_{wg} is the wind power output; $K_1(s)$, $K_2(s)$, $M_1(s)$, $M_2(s)$, and $M_{\mathrm{ASL}}(s)$ are the transfer functions of MPC controller, governor-turbine model, and ASL model, respectively; P_{vpp} is the power output of VPP; and P_{asl} is the power consumption of ASL. Note that some of the variables are defined when they appear in the following equations. Power injection in the RPS system consists $P_{m,1}$, $P_{nl,1}$, and $P_{s,1}$. Power injection in the PPS system consists of $P_{m,2}$, P_{wg}, P_{asl}, $P_{nl,2}$, and $P_{s,2}$.

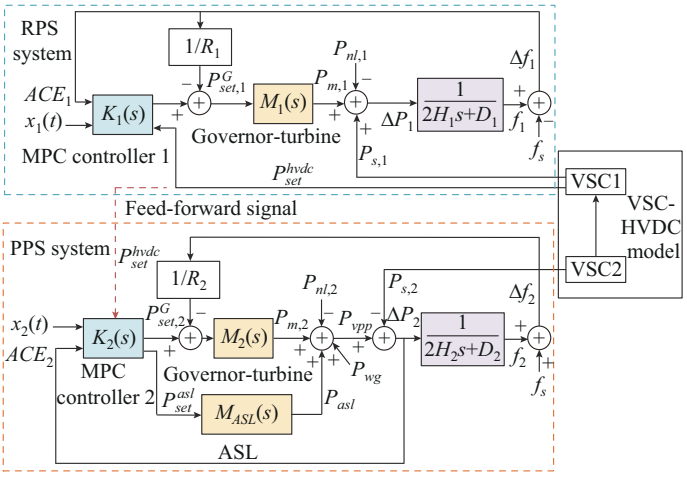

Fig. 2. SFC model for two-terminal HVDC system.

Let the RPS system and PPS system be denoted by the subscripts $i=1$ and $i=2$, respectively. Then, the dynamics of the i^{th} system can be expressed as:

$$\dot{f}_i = \frac{1}{2H_i}\Delta P_i - \frac{D_i}{2H_i} f_i \tag{1}$$

$$\dot{P}_{mH,i} = \frac{P_{v,i} - P_{mH,i}}{T_{CH,i}} \tag{2}$$

$$\dot{P}_{mL,i} = \frac{P_{mH,i} - P_{mL,i}}{T_{RH,i}} \tag{3}$$

$$\dot{P}_{v,i} = \frac{P^G_{set,i} - \dfrac{\Delta f_i}{R_i} - P_{v,i}}{T_{g,i}} \tag{4}$$

$$\Delta P_1 = P_{m,1} + P_{s,1} - P_{nl,1} \tag{5}$$

$$\Delta P_2 = P_{m,2} + P_{wg} - P_{asl} - P_{nl,2} - P_{s,2} = P_{vpp} - P_{s,2} \tag{6}$$

$$P_{m,i} = F_{HP,i} P_{mH,i} + F_{LP,i} P_{mL,i} \tag{7}$$

where f_i, Δf_i, and f_s are the frequency, frequency deviation, and standard value, respectively; H_i and D_i are the synchronous machine inertia and machine damping coefficient, respectively; ΔP_i is the power imbalance; R_i is the speed drop; $P_{m,i}$ and $P_{v,i}$ are the mechanical outputs of the valve position; $P_{mH,i}$ and $P_{mL,i}$ are the mechanical outputs of the high- and low-pressure cylinders, respectively; $T_{g,i}$ is the time constant of the governor; $T_{CH,i}$ and $T_{RH,i}$ are the time instances of the high- and low-pressure cylinders, respectively; and $F_{HP,i}$ and $F_{LP,i}$ are the proportionality coefficients of the high- and low-pressure cylinders, respectively.

The objectives of the RPS system and PPS system are to minimize Δf_1 and ΔP_2, respectively. Therefore, ACE_1 and ACE_2 are selected as:

$$ACE_1 = \Delta f_1^2 = \left(f_s - f_1\right)^2 \tag{8}$$

$$ACE_2 = \Delta P_2^2 = \left(P_{vpp} - P_{s,2}\right)^2 \tag{9}$$

B. VSC-HVDC Model

A schematic diagram of the two-terminal VSC-HVDC link is shown in Fig. 3.

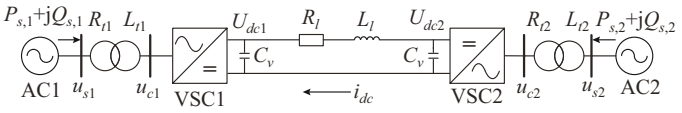

Fig. 3. Schematic diagram of two-terminal VSC-HVDC link.

As widely reported in [25] and [26], the dynamics of a VSC-HVDC system in the *dq* rotating frame can be expressed as follows, where the Park transformation is amplitude invariant.

$$\frac{\mathrm{d}i_d}{\mathrm{d}t} = \frac{-R_t i_d - \omega L_t i_q + u_{sd} - u_d}{L_t} \tag{10}$$

$$\frac{\mathrm{d}i_q}{\mathrm{d}t} = \frac{-R_t i_q + \omega L_t i_d - u_q}{L_t} \tag{11}$$

$$\frac{\mathrm{d}U_{dc1}}{\mathrm{d}t} = \frac{3K_1\left(i_{d1}\cos\delta_1 + i_{q1}\sin\delta_1\right)}{2C_v - i_{dc}} \tag{12}$$

$$\frac{\mathrm{d}U_{dc2}}{\mathrm{d}t} = \frac{3K_2\left(i_{d2}\cos\delta_2 + i_{q2}\sin\delta_2\right)}{2C_v + i_{dc}} \tag{13}$$

$$\frac{\mathrm{d}i_{dc}}{\mathrm{d}t} = \frac{U_{dc1} - U_{dc2} - R_l i_{dc}}{L_l} \tag{14}$$

$$P_s = 1.5 u_{sd} i_d \tag{15}$$

$$Q_s = 1.5 u_{sd} i_q \tag{16}$$

where P_s and Q_s are the active power and reactive power injected into the AC system, respectively; u_s and u_c are the voltages of the AC system and VSC, respectively; U_{dc} is the DC voltage of the VSC; u_{sd} is the *d*-axis component of u_s; R_t and L_t are the resistance and inductance of the transformer,

respectively; R_l and L_l are the resistance and inductance of the transmission line, respectively; C_v is the capacitance at the DC side; u_d, i_d, u_q, and i_q are the d- and q-axis components of the voltage and current of the VSC, respectively; δ is the angle between u_c and u_s; ω is the angular frequency of the AC system; and K is the utilization rate of the DC voltage, which is the ratio of the maximum amplitude of the fundamental wave of the AC voltage that the inverter can output to the input DC voltage (a coefficient related to the modulation method, K = 0.866 in this paper.

VSC-HVDC control consists of fast inner current control and slower outer control. The outer control supplies the reference values of the current $i_{d,ref}$ and $i_{q,ref}$. The inner control adjusts i_d and i_q to follow the reference values. The outer control is based on PI control and has four optional control objectives for each VSC: P_s, U_{dc}, Q_s, and u_s.

Since the inner current control is much faster than the outer control, i_d and i_q can be directly assumed to be equal to their reference values $i_{d,ref}$ and $i_{q,ref}$, respectively [27]. Under this assumption, the complex control of the VSCs can be simplified to PI control, which reduces the order of the control system and changes it into a linear control system. This can greatly improve the simulation efficiency and will not affect the simulation accuracy because the period to complete an inner control process is much shorter than a simulation step in this paper.

C. ASL Model

ASLs are typical flexible loads based on continuous power control by a self-saturable reactor. A dynamic model for an ASL with a self-saturable reactor has been detailed in our previous work [7]. Therefore, the dynamics of an ASL can be characterized by the state space model in [7]:

$$\begin{bmatrix} \dot{I}_{bk} \\ \dot{I}_c^{asl} \\ \dot{I}_d^{asl} \end{bmatrix} = \begin{bmatrix} \dfrac{-r_{bk}}{L_{bk}} & \dfrac{-R_c}{L_{bk}} & 0 \\ \dfrac{1}{R_c^{asl}C_{bk}} & \dfrac{-1}{R_c^{asl}C_{bk}} & 0 \\ 0 & \dfrac{-k_c}{\tau_d R_d^{asl}} & \dfrac{-1}{\tau_d} \end{bmatrix} \begin{bmatrix} I_{bk} \\ I_c^{asl} \\ I_d^{asl} \end{bmatrix} + \begin{bmatrix} \dfrac{E_{bk}}{L_{bk}} \\ 0 \\ 0 \end{bmatrix} d + \begin{bmatrix} \dfrac{E_{bk}}{L_{bk}} \\ 0 \\ \dfrac{U_{d0}^{asl} - E_d^{asl}}{\tau_d R_d^{asl}} \end{bmatrix} \tag{17}$$

$$U_d^{asl} = U_{d0}^{asl} - k_c I_c^{asl} \tag{18}$$

$$P_{asl} = U_d^{asl} I_d^{asl} \tag{19}$$

where I_{bk}, E_{bk}, C_{bk}, L_{bk}, and r_{bk} are the current, power supply voltage, capacitance, inductance, and resistance of the buck converter in the ASL, respectively; I_c^{asl}, R_c^{asl}, and k_c are the current, resistance, and control coefficient of the control winding in the ASL, respectively; I_d^{asl}, U_d^{asl}, R_d^{asl}, E_d^{asl}, and τ_d are the DC current, DC voltage, resistance, electromotive force, and time constant of the potline in the ASL, respectively; d is the duty cycle of the buck converter in ASL; and U_{d0}^{asl} is the rated value of the DC voltage of the potline.

ASL control is based on the DC current control scheme, which aims to stabilize the DC I_d^{asl} at its reference value I_{ref}^{asl} in smelter loads [28], [29].

P_{set}^{asl} can be converted to I_{ref}^{asl} by (20), which is based on the ASL model [30]. Then, I_d^{asl} can be controlled to I_{ref}^{asl} through the DC control scheme. Consequently, P_{asl} will also be controlled to P_{set}^{asl}.

$$I_{ref}^{asl} = \frac{\sqrt{\left(P_{set}^{asl}\right)^2 + 4R_d^{asl}P_{set}^{asl}} - E_d^{asl}}{2R_d^{asl}} \tag{20}$$

D. Wind Farm Model

In this paper, P_{wg} is assumed to be composed of the forecasted wind power P_{wg}^{for} and forecasting error e_{wg}. The forecasted wind output is determined by the wind farm parameters and wind speed v [31]. The forecasting error obeys the standard normal distribution $N(0, \sigma^2)$ [32].

$$P_{wg} = P_{wg}^{for} + e_{wg} \tag{21}$$

$$P_{wg}^{for} = \frac{1}{2} C_p \rho A v^3 \tag{22}$$

where C_p is the coefficient of performance of the rotor; ρ is the mass density of air; and A is the swept area of the blades.

IV. MPC-based Control Schemes

A. MPC Controller in RPS System

MPC controller 1 is designed to calculate the optimal control commands with the objective of minimizing ACE_1 in the RPS system. To improve control performance, the grid constraints of the RPS system are included in the prediction model.

1) State Space Model of Generators

As mentioned in Section III-A, the aggregated single-unit model is expressed in (1) - (4). To consider the grid constraints, the aggregated model should be expanded to a model of multiple individual generators.

Let the subscript j denote the serial number of the j^{th} individual generator. The state equation of the j^{th} generator can be expressed as:

$$\dot{\boldsymbol{x}}_{Gj} = \begin{bmatrix} -1/T_{g,j} & 0 & 0 & 0 & 1/\left(T_{g,j}R_j\right) \\ 1/T_{CH,j} & -1/T_{CH,j} & 0 & 0 & 0 \\ 0 & 1/T_{RH,j} & -1/T_{RH,j} & 0 & 0 \\ 0 & 0 & 0 & 0 & \omega_s \\ 0 & F_{HP,j}/\left(2H_j\right) & F_{LP,j}/\left(2H_j\right) & 0 & -D_j/\left(2H_j\right) \end{bmatrix} \boldsymbol{x}_{Gj} + \begin{bmatrix} 1/T_{g,j} \\ 0 \\ 0 \\ 0 \\ 0 \end{bmatrix} \boldsymbol{u}_{Gj} + \begin{bmatrix} 0 \\ 0 \\ 0 \\ 0 \\ -1/\left(2H_j\right) \end{bmatrix} \boldsymbol{P}_{ej} + \begin{bmatrix} -\omega_s/\left(T_{g,j}R_j\right) \\ 0 \\ 0 \\ -\omega_s \\ 0 \end{bmatrix} \tag{23}$$

where $\boldsymbol{x}_{Gj} = [P_{vj}, P_{mHj}, P_{mLj}, \delta_j, \omega_j]^{\mathrm{T}}$; $\boldsymbol{u}_{Gj} = \boldsymbol{P}_{set,j}^{G}$; $\boldsymbol{P}_{ej}$ is the electrical power of the j^{th} generator; and ω_s is the base value of the angular speed. The other parameters have the same meaning as those in the aggregated model.

Equation (23) can be written in condensed form as:

$$\dot{\boldsymbol{x}}_{Gj} = \boldsymbol{A}_{Gj}\boldsymbol{x}_{Gj} + \boldsymbol{B}_{Gj}\boldsymbol{u}_{Gj} + \boldsymbol{C}_{Gj}\boldsymbol{P}_{ej} + \boldsymbol{D}_{Gj} \tag{24}$$

The state equation of all of the conventional generators in the system is:

$$\dot{\boldsymbol{x}}_G=\boldsymbol{A}_G\boldsymbol{x}_G+\boldsymbol{B}_G\boldsymbol{u}_G+\boldsymbol{C}_G\boldsymbol{P}_e+\boldsymbol{D}_G \tag{25}$$

where $\boldsymbol{x}_G=[\boldsymbol{x}_{G1}^{\mathrm{T}},\boldsymbol{x}_{G2}^{\mathrm{T}},\ldots,\boldsymbol{x}_{Gn}^{\mathrm{T}}]$; $\boldsymbol{u}_G=[\boldsymbol{u}_{G1}^{\mathrm{T}},\boldsymbol{u}_{G2}^{\mathrm{T}},\ldots,\boldsymbol{u}_{Gn}^{\mathrm{T}}]$; $\boldsymbol{P}_e=[\boldsymbol{P}_{e1},\boldsymbol{P}_{e2},\ldots,\boldsymbol{P}_{en}]$; $\boldsymbol{A}_G=\mathrm{diag}(\boldsymbol{A}_{Gj})$; $\boldsymbol{B}_G=\mathrm{diag}(\boldsymbol{B}_{Gj})$; $\boldsymbol{C}_G=\mathrm{diag}(\boldsymbol{C}_{Gj})$; and $\boldsymbol{D}_G=\mathrm{diag}(\boldsymbol{D}_{Gj})$.

2) Prediction Model Considering Grid Constraints

Considering the topological information of the power grid, the DC power flow is used for the power network equation:

$$\boldsymbol{P}=\boldsymbol{B}\boldsymbol{\theta} \tag{26}$$

where $\boldsymbol{B}$ is the admittance matrix of the DC power grid; $\boldsymbol{P}$ is the active power in each node; and $\boldsymbol{\theta}$ is the phase angle of the voltage in each node.

Equation (26) can be expanded as:

$$\begin{bmatrix}\boldsymbol{P}_e\\ \boldsymbol{P}_l\end{bmatrix}=\begin{bmatrix}\boldsymbol{B}_{ee} & \boldsymbol{B}_{el}\\ \boldsymbol{B}_{le} & \boldsymbol{B}_{ll}\end{bmatrix}\begin{bmatrix}\boldsymbol{\theta}_e\\ \boldsymbol{\theta}_l\end{bmatrix} \tag{27}$$

where the subscripts e and l correspond to the parameters of the generator and load nodes, respectively.

The relationship between the phase angle of the voltage in the bus near the generator and the angle of the rotor of the generator is:

$$\boldsymbol{P}_e=\frac{\boldsymbol{\delta}-\boldsymbol{\theta}_e}{\boldsymbol{X}_d'} \tag{28}$$

where $\boldsymbol{X}_d'$ is the transient reactance of the unit; $\boldsymbol{\delta}$ is the rotor of the generator; and $\boldsymbol{\theta}_e$ is the bus near the generator.

Combining (27) and (28), the electrical power vector $\boldsymbol{P}_{e1}$ in the RPS system can be expressed as:

$$\boldsymbol{P}_{e1}=\boldsymbol{F}_1\boldsymbol{\delta}_1+\boldsymbol{G}_1\boldsymbol{P}_{l1} \tag{29}$$

$$\boldsymbol{F}_1=\left[\boldsymbol{I}_1+\left(\boldsymbol{B}_{ee,1}-\boldsymbol{B}_{el,1}\boldsymbol{B}_{ll,1}^{-1}\boldsymbol{B}_{le,1}\right)\boldsymbol{X}_{d1}'\right]^{-1}\left(\boldsymbol{B}_{ee,1}-\boldsymbol{B}_{el,1}\boldsymbol{B}_{ll,1}^{-1}\boldsymbol{B}_{le,1}\right) \tag{30}$$

$$\boldsymbol{G}_1=\left[\boldsymbol{I}_1+\left(\boldsymbol{B}_{ee,1}-\boldsymbol{B}_{el,1}\boldsymbol{B}_{ll,1}^{-1}\boldsymbol{B}_{le,1}\right)\boldsymbol{X}_{d1}'\right]^{-1}\boldsymbol{B}_{el,1}\boldsymbol{B}_{ll,1}^{-1} \tag{31}$$

Because EDCPS is included in the control scheme, the power injection of the VSC1 node is also a control variable. Then, (29) can be expressed as:

$$\boldsymbol{P}_{e1}=\boldsymbol{F}_1\boldsymbol{\delta}_1+\boldsymbol{G}_1\boldsymbol{P}_{l,1}=\boldsymbol{F}_1\boldsymbol{\delta}_1+[G_{hvdc,1}\quad G_{nl,1}][P_{s,1}\quad P_{nl,1}]^{\mathrm{T}} \tag{32}$$

where $G_{hvdc,1}$ and $G_{nl,1}$ are the coefficients of $P_{s,1}$ and $P_{nl,1}$, respectively.

Since $P_{s,1}$ is a state variable rather than a control variable, it can be replaced with the target value P_{set}^{hvdc}. Substituting (32) into (25), the state space model of the RPS system considering grid constraints and HVDC participation can be expressed as:

$$\dot{\boldsymbol{x}}_1=\boldsymbol{A}_1\boldsymbol{x}_1+\boldsymbol{B}_1\boldsymbol{u}_1+\boldsymbol{D}_1 \tag{33}$$

where $\boldsymbol{x}_1=[P_{v,1}\quad P_{mH,1}\quad P_{mL,1}\quad \delta_1\quad \omega_1]^{\mathrm{T}}$; $\boldsymbol{u}_1=[P_{set,1}^{G}\quad P_{set}^{hvdc}]^{\mathrm{T}}$;

$$\boldsymbol{A}_1=\begin{bmatrix}-1/T_{g,1} & 0 & 0 & 0 & 1/\left(T_{g,1}R_1\right)\\ 1/T_{CH,1} & -1/T_{CH,1} & 0 & 0 & 0\\ 0 & 1/T_{RH,1} & -1/T_{RH,1} & 0 & 0\\ 0 & 0 & 0 & 0 & \omega_s\\ 0 & F_{HP,1}/\left(2H_1\right) & F_{LP,1}/\left(2H_1\right) & -F_1/\left(2H_1\right) & -D_1/\left(2H_1\right)\end{bmatrix};$$

$$\boldsymbol{B}_1=\begin{bmatrix}1/T_{g,1} & 0\\ 0 & 0\\ 0 & 0\\ 0 & 0\\ 0 & -G_{hvdc,1}/\left(2H_1\right)\end{bmatrix};\ \text{and}\ \boldsymbol{D}_1=\begin{bmatrix}-\omega_s/\left(T_{g,1}R_1\right)\\ 0\\ 0\\ -\omega_s\\ -G_{nl,1}P_{nl,1}/\left(2H_1\right)\end{bmatrix}.$$

Note that the grid constraints mentioned here include the DC power flow (27) and an equation for the angle of the rotor of the generator (28), where the two equations are combined to derive the power flow equation (29). The power flow equation includes the grid constraints owing to the presence of the admittance matrix $\boldsymbol{B}_1$ in the coefficient matrices $\boldsymbol{F}_1$ and $\boldsymbol{G}_1$. Then, because $\boldsymbol{F}_1$ and $\boldsymbol{G}_1$ are implicit in the matrices $\boldsymbol{A}_1$ and $\boldsymbol{B}_1$ in (33) via the power flow equation, the grid constraints are also included in the state space model.

Discretizing the state space model in (33) with the sample period T_s, we obtain the prediction model of the RPS system as:

$$\boldsymbol{x}_1[k+1]=\boldsymbol{A}_{d1}\boldsymbol{x}_1[k]+\boldsymbol{B}_{d1}\boldsymbol{u}_1[k]+\boldsymbol{D}_{d1} \tag{34}$$

where $\boldsymbol{A}_{d1}=\mathrm{e}^{\boldsymbol{A}_1T_s}$; $\boldsymbol{B}_{d1}=\int_0^{T_s}\mathrm{e}^{\boldsymbol{A}_1T_s}\mathrm{d}t\boldsymbol{B}_1$; $\boldsymbol{D}_{d1}=\int_0^{T_s}\mathrm{e}^{\boldsymbol{A}_1T_s}\mathrm{d}t\boldsymbol{D}_1$; and $\boldsymbol{A}_{d1}$, $\boldsymbol{B}_{d1}$, and $\boldsymbol{D}_{d1}$ are the system matrices derived from $\boldsymbol{A}_1$, $\boldsymbol{B}_1$, and $\boldsymbol{D}_1$ in (33) after discretization with the sampling time T_s. The notation $f[k]=f(kT_s)$ is used throughout this paper. Since the state space model in (33) considers grid constraints, they are also included in the discretized prediction model, which means that the predicted state variables also satisfy the constraints.

Equation (34) is the prediction model of all state variables for the generators. Accordingly, a prediction of the frequency ω_1 ($f=\omega$ in p.u.) can be obtained with the output matrix $\boldsymbol{C}_{d1}=[0,0,0,0,1]$:

$$\boldsymbol{y}_1[k+1]=\boldsymbol{C}_{d1}\boldsymbol{x}_1[k+1]=\boldsymbol{C}_{d1}\boldsymbol{A}_{d1}\boldsymbol{x}_1[k]+\boldsymbol{C}_{d1}\boldsymbol{B}_{d1}\boldsymbol{u}_1[k]+\boldsymbol{C}_{d1}\boldsymbol{D}_{d1} \tag{35}$$

3) Receding Horizon Optimization

The optimization of the RPS system aims to minimize ACE_1, which is determined by the frequency deviation:

$$ACE_1=\left(\boldsymbol{\omega}_s-\boldsymbol{y}_1[k+1]\right)^{\mathrm{T}}\left(\boldsymbol{\omega}_s-\boldsymbol{y}_1[k+1]\right) \tag{36}$$

where $\boldsymbol{\omega}_s$ is the diagonal matrix of standard value of rotor angular velocity.

The receding horizon optimization can be formulated as a quadratic programming (QP) problem:

$$\begin{aligned}\min J_1=&\left(\boldsymbol{\omega}_s-\boldsymbol{y}_1[k+1]\right)^{\mathrm{T}}\boldsymbol{Q}_{11}\left(\boldsymbol{\omega}_s-\boldsymbol{y}_1[k+1]\right)+\\ &\left(\boldsymbol{u}_1[k]-\boldsymbol{u}_1[k-1]\right)^{\mathrm{T}}\boldsymbol{Q}_{12}\left(\boldsymbol{u}_1[k]-\boldsymbol{u}_1[k-1]\right)\end{aligned} \tag{37}$$

s.t.

$$\boldsymbol{y}_1[k+1]=\boldsymbol{C}_1\boldsymbol{A}_{d1}\boldsymbol{x}_1[k]+\boldsymbol{C}_1\boldsymbol{B}_{d1}\boldsymbol{u}_1[k]+\boldsymbol{C}_1\boldsymbol{D}_{d1} \tag{38}$$

$$\boldsymbol{u}_{1,\min}\le\boldsymbol{u}_1[k]\le\boldsymbol{u}_{1,\max} \tag{39}$$

$$\boldsymbol{u}_1[k]-\boldsymbol{u}_1[k-1]\le\Delta\boldsymbol{u}_{1,\max} \tag{40}$$

The control variable is $\boldsymbol{u}_1=[P_{set,1}^{G},P_{set}^{hvdc}]^{\mathrm{T}}$. The objective function in (37) consists of ACE_1 and the penalty term for the incremental control variable, where $\boldsymbol{Q}_{11}$ and $\boldsymbol{Q}_{12}$ are the weight matrices. The constraint in (38) is an equation for the prediction model considering the grid constraints. The con-

straint in (39) expresses the amplitude constraints of the control variables, which consist of the lower and upper limits of the output of the generator and HVDC power modulation. The constraint in (40) is the ramping constraint of the output of the generator and HVDC power modulation.

4) Determination of MPC Parameters

This subsection introduces a method for determining the control step T_{c1}, prediction horizon T_{p1}, and weight matrices ($\boldsymbol{Q}_{11}$, $\boldsymbol{Q}_{12}$) of MPC controller 1 in the RPS system, where the control step and prediction horizon are constant and the weight matrices are time-varying owing to feedback control deviations.

In the SFC process, the AGC period is usually set to be 4-8 s. As an AGC controller, the control step of the proposed MPC controller should also be within this range to match the remote terminal unit (RTU) in the AGC units. In this paper, the control step of the MPC controller in the RPS system is selected to be $T_{c1}=5$ s.

Since the prediction model in (34) is obtained by the discretization of the state space model of the RPS system with the sample period T_s, the prediction is one-step, and the prediction horizon T_{p1} is equal to the sample period T_s. In this study, the prediction horizon of the MPC controller in the RPS system is selected to be $T_{p1}=10$ s.

In the objective function, the weight matrices $\boldsymbol{Q}_{11}$ and $\boldsymbol{Q}_{12}$ represent the priority of the elimination of ACE_1 and the penalty on the control variables, respectively. In order to ensure transient performance, $\boldsymbol{Q}_{11}$ is much larger than $\boldsymbol{Q}_{12}$. Under this premise, if $\boldsymbol{Q}_{11}$ is kept constant, the variation in $\boldsymbol{Q}_{12}$ can also affect the performance of the MPC controller. If $\boldsymbol{Q}_{12}$ becomes larger, there will be a greater penalty on the increment of the control variables, which leads to conservative control signals. On the contrary, a smaller $\boldsymbol{Q}_{12}$ leads to aggressive control signals.

Since $\boldsymbol{Q}_{11}$ and $\boldsymbol{Q}_{12}$ can affect control performance, they should be selected properly. In this paper, $\boldsymbol{Q}_{11}$ is kept constant, and $\boldsymbol{Q}_{12}$ varies with the feedback frequency deviations Δf_1:

$$\boldsymbol{Q}_{12}=\boldsymbol{Q}_{12}^{s}-\boldsymbol{K}_{q1}\Delta f_1 \tag{41}$$

where $\boldsymbol{Q}_{12}^{s}$ and $\boldsymbol{K}_{q1}$ are the standard value and droop coefficient of $\boldsymbol{Q}_{12}$, respectively.

Compared with constant weight matrices, time-varying weight matrices make the control more flexible and reasonable. When the deviation is large, the control is more aggressive to obtain better transient performance. When the deviation becomes small, the control is more conservative to obtain high stability, which smoothens the frequency recovery curve and reduces the adverse effects on the VSC-HVDC system caused by dramatic changes.

B. MPC Controller in PPS System

The industrial power grid in the PPS system is integrated as a VPP model. MPC controller 2 is designed to calculate the optimal control commands with the objective of minimizing ACE_2. The adverse effects caused by the urgency of EDCPS are reduced by including a feed-forward signal in the prediction model. The uncertainty associated with wind power is considered by a chance-constraint method [33], [34].

1) Prediction Model Including a Feed-forward Signal

According to the derivation in Section IV-A, the electrical power vector $\boldsymbol{P}_{e2}$ in the PPS system can be expressed as:

$$\boldsymbol{P}_{e2}=\boldsymbol{F}_2\boldsymbol{\delta}_2+\boldsymbol{G}_2\boldsymbol{P}_{l,2}=\boldsymbol{F}_2\boldsymbol{\delta}_2+[G_{asl}\quad G_{hvdc,2}\quad G_{wg}\quad G_{nl,2}][P_{asl}\quad P_{s,2}\quad P_{wg}\quad P_{nl,2}]^{\mathrm{T}} \tag{42}$$

where G_{asl}, $G_{hvdc,2}$, G_{wg}, and $G_{nl,2}$ are the coefficients of P_{asl}, $P_{s,2}$, P_{wg}, and $P_{nl,2}$, respectively.

To minimize the power imbalance in the PPS system caused by EDCPS, the EDCPS command P_{set}^{hvdc} calculated in the RPS system will be sent to the PPS system in advance as a feed-forward signal. Then, the power injection $P_{s,2}$ can be replaced by the EDCPS command signal P_{set}^{hvdc}. In this way, the EDCPS command is included in the prediction model as a feed-forward signal.

According to (33), the state space model of the PPS system can be expressed as:

$$\dot{\boldsymbol{x}}_2=\boldsymbol{A}_2\boldsymbol{x}_2+\boldsymbol{B}_2\boldsymbol{u}_2+\boldsymbol{D}_2 \tag{43}$$

where $\boldsymbol{x}_2=[P_{v,2}\quad P_{mH,2}\quad P_{mL,2}\quad \delta_2\quad \omega_2]^{\mathrm{T}}$; $\boldsymbol{u}_2=[P_{set,2}^{G}\quad P_{set}^{asl}]^{\mathrm{T}}$;

$$\boldsymbol{A}_2=\begin{bmatrix} -1/T_{g,2} & 0 & 0 & 0 & 1/(T_{g,2}R) \\ 1/T_{CH,2} & -1/T_{CH,2} & 0 & 0 & 0 \\ 0 & 1/T_{RH,2} & -1/T_{RH,2} & 0 & 0 \\ 0 & 0 & 0 & 0 & \omega_s \\ 0 & F_{HP,2}/(2H_2) & F_{IP,2}/(2H_2) & -F_2/(2H_2) & -D_2/(2H_2) \end{bmatrix};$$

$$\boldsymbol{D}_2=\begin{bmatrix} -\omega_s/(T_{g,2}R_2) \\ 0 \\ 0 \\ -\omega_s \\ \left(-G_{hvdc,2}P_{set}^{hvdc}-G_{wg}P_{wg}^{for}-G_{nl,2}P_{nl,2}\right)/(2H_2) \end{bmatrix};\quad \text{and}\quad \boldsymbol{B}_2=\begin{bmatrix} 1/T_{g,2} & 0 \\ 0 & 0 \\ 0 & 0 \\ 0 & 0 \\ 0 & -G_{asl}/(2H_2) \end{bmatrix}.$$

The control variable $\boldsymbol{u}_2=[P_{set,2}^{G}, P_{set}^{asl}]^{\mathrm{T}}$ is the power set point of the generators and ASLs. P_{set}^{hvdc}, P_{wg}^{for}, and $P_{nl,2}$ are included in the matrix $\boldsymbol{D}_2$.

Discretizing the state space model in (43) with the sample period T_s, we can obtain the prediction model of the PPS system as:

$$\boldsymbol{x}_2[k+1]=\boldsymbol{A}_{d2}\boldsymbol{x}_2[k]+\boldsymbol{B}_{d2}\boldsymbol{u}_2[k]+\boldsymbol{D}_{d2} \tag{44}$$

where $\boldsymbol{A}_{d2}=\mathrm{e}^{\boldsymbol{A}_2T_s}$; $\boldsymbol{B}_{d2}=\int_0^{T_s}\mathrm{e}^{\boldsymbol{A}_2T_s}\mathrm{d}t\boldsymbol{B}_2$; and $\boldsymbol{D}_{d2}=\int_0^{T_s}\mathrm{e}^{\boldsymbol{A}_2T_s}\mathrm{d}t\boldsymbol{D}_2$.

Equation (44) is the prediction model of all state variables of the generators. The prediction of the frequency f_2 can be obtained by the output matrix $\boldsymbol{C}_{d2}=[0, 0, 0, 0, 1]$:

$$\boldsymbol{y}_2[k+1]=\boldsymbol{C}_{d2}\boldsymbol{x}_2[k+1]=\boldsymbol{C}_{d2}\boldsymbol{A}_{d2}\boldsymbol{x}_2[k]+\boldsymbol{C}_{d2}\boldsymbol{B}_{d2}\boldsymbol{u}_2[k]+\boldsymbol{C}_{d2}\boldsymbol{D}_{d2} \tag{45}$$

2) Receding Horizon Optimization Including a Chance Constraint

In the PPS system, self-owned generators, wind farms, ASLs, and normal loads can be regarded as a VPP with P_{vpp}. ACE_2 is decided by the difference between P_{vpp} and $P_{s,2}$. Here, $P_{s,2}$ is replaced with P_{set}^{hvdc} to include the feed-forward signal in ACE_2, which can be reformulated as:

$$ACE_2=\left(P_{vpp}-P_{set}^{hvdc}\right)^2=\left(P_{wg}+P_{m,2}-P_{asl}-P_{l,2}-P_{set}^{hvdc}\right)^2 \tag{46}$$

As mentioned in Section III, P_{wg} consists of P_{wg}^{for} and r_{wg}, where $r_{wg}\sim N(0,\ \sigma^2)$. The prediction model should be modified to include r_{wg}.

Substituting (21) into (41) and (42), the prediction model involving the random variable r_{wg} can be reformulated as:

$$\tilde{\boldsymbol{x}}_2[k+1]=\boldsymbol{x}_2[k+1]+\boldsymbol{R}_{N_d}e_{wg} \tag{47}$$

$$\tilde{\boldsymbol{y}}_2[k+1]=\boldsymbol{y}_2[k+1]+\boldsymbol{C}_{d2}\boldsymbol{R}_{N_d}e_{wg} \tag{48}$$

where $\boldsymbol{R}_{N_d}=\mathrm{e}^{\boldsymbol{A}_2T_s}\mathrm{d}t\boldsymbol{R}_N$ and $\boldsymbol{R}_N=\left[0,0,0,0,-G_{wg}/\left(2H_2\right)\right]^{\mathrm{T}}$.

Including e_{wg}, ACE_2 can be formulated as:

$$ACE_2=\left[\left(P_{wg}^{for}+P_{m,2}-P_{asl}-P_{l,2}-P_{set}^{hvdc}\right)-e_{wg}\right]^2=\left(\Delta P_2^{for}-e_{wg}\right)^2 \tag{49}$$

The receding horizon optimization in the PPS system can be formulated as a QP problem with a random variable:

$$\begin{aligned}\min\ J_2=&\boldsymbol{Q}_{21}\left(\Delta P_2^{for}-e_{wg}\right)^2+\\&\left(\boldsymbol{u}_2[k]-\boldsymbol{u}_2[k-1]\right)^{\mathrm{T}}\boldsymbol{Q}_{22}\left(\boldsymbol{u}_2[k]-\boldsymbol{u}_2[k-1]\right)\end{aligned} \tag{50}$$

s.t.

$$\boldsymbol{y}_2[k+1]=\boldsymbol{C}_{d2}\boldsymbol{A}_{d2}\boldsymbol{x}_2[k]+\boldsymbol{C}_{d2}\boldsymbol{B}_{d2}\boldsymbol{u}_2[k]+\boldsymbol{C}_{d2}\boldsymbol{D}_{d2} \tag{51}$$

$$\Delta P_2^{for}=P_{set}^{hvdc}-\left(P_{wg}^{for}+P_{m,2}-P_{asl}-P_{nl,2}\right) \tag{52}$$

$$\boldsymbol{u}_{2,\min}\le\boldsymbol{u}_2[k]\le\boldsymbol{u}_{2,\max} \tag{53}$$

$$\boldsymbol{u}_2[k]-\boldsymbol{u}_2[k-1]\le\Delta\boldsymbol{u}_{2,\max} \tag{54}$$

$$\boldsymbol{f}_{\min}\le\boldsymbol{y}_2[k+1]+\boldsymbol{C}_{d2}\boldsymbol{R}_{N_d}e_{wg}\le\boldsymbol{f}_{\max} \tag{55}$$

The control variable is $\boldsymbol{u}_2=[P_{set,2}^G, P_{set}^{asl}]^{\mathrm{T}}$. The objective function in (50) consists of ACE_2 and the penalty term for the incremental control variable. The constraint in (51) is an equation for the prediction model considering the grid constraints. The constraint in (52) is the power imbalance equation of the PPS system. The constraint in (53) expresses the amplitude constraints of the control variables, which consist of the lower and upper limits of the output of the generator and the power consumed by the ASL. The constraint in (54) is the ramping constraint of the output of the generator and the ASL power regulation. The constraint in (55) represents the lower and upper bounds of the frequency considering e_{wg}, where $\boldsymbol{f}_{\max}$ and $\boldsymbol{f}_{\min}$ are the upper and lower bounds, respectively.

e_{wg} is included in the objective function in (50) and the constraint in (55). Therefore, (50)-(55) are a stochastic optimization problem and is not tractable in its current form. To convert this stochastic optimization problem into a deterministic optimization problem, a formulation for the chance constraints is adopted. Since e_{wg} obeys $N(0,\ \sigma^2)$, ACE_2 in (50) can be reformulated using the mathematical expectation:

$$\begin{aligned}ACE_2=&E\left(\left(\Delta P_2^{for}-e_{wg}\right)^2\right)=E\left(\left(\Delta P_2^{for}\right)^2\right)-2E\left(\Delta P_2^{for}\right)E\left(e_{wg}\right)+\\&E\left(e_{wg}^2\right)=\left(\Delta P_2^{for}\right)^2-2\Delta P_2^{for}E\left(e_{wg}\right)+E^2\left(e_{wg}\right)+D\left(e_{wg}\right)=\\&\left(\Delta P_2^{for}\right)^2-2\Delta P_2^{for}0+0^2+D\left(e_{wg}\right)=\left(\Delta P_2^{for}\right)^2+\sigma^2\end{aligned} \tag{56}$$

where $E(\cdot)$ is the mathematical expectation of $(\cdot)$; and $D(\cdot)$ is the variance of $(\cdot)$.

Equation (55) can be expressed as a probabilistic constraint with a predescribed probability β:

$$P_r\left\{\boldsymbol{f}_{\min}\le\boldsymbol{y}_2[k+1]+\boldsymbol{C}_{d2}\boldsymbol{R}_{N_d}e_{wg}\le\boldsymbol{f}_{\max}\right\}\ge\beta \tag{57}$$

According to probability theory, the frequency prediction $\boldsymbol{y}_2[k+1]+\boldsymbol{C}_{d2}\boldsymbol{R}_{N_d}e_{wg}$ in (57) also obeys a normal distribution $N(f_0,\ (\boldsymbol{C}_{d2}\boldsymbol{R}_{N_d})^{\mathrm{T}}(\boldsymbol{C}_{d2}\boldsymbol{R}_{N_d})\sigma^2)$.

The probabilistic constraint in (47) needs to be reformulated into a deterministic constraint. This can be done by interpreting it as a tightened version of the original constraint, where tightening represents a security margin against uncertainty:

$$\boldsymbol{f}_{\min}+\boldsymbol{\Omega}_\beta\le\boldsymbol{y}_2[k+1]\le\boldsymbol{f}_{\max}-\boldsymbol{\Omega}_\beta \tag{58}$$

where $\boldsymbol{\Omega}_\beta$ is the uncertainty margin.

Then, (50)-(55) can be reformulated as a deterministic QP problem:

$$\begin{cases}\min J_2=\boldsymbol{Q}_{21}\left[\left(\Delta P_2^{for}\right)^2+\sigma^2\right]+\\\qquad\left(\boldsymbol{u}_2[k]-\boldsymbol{u}_2[k-1]\right)^{\mathrm{T}}\boldsymbol{Q}_{22}\left(\boldsymbol{u}_2[k]-\boldsymbol{u}_2[k-1]\right)\\\text{s.t. }\ \boldsymbol{y}_2[k+1]=\boldsymbol{C}_{d2}\boldsymbol{A}_{d2}\boldsymbol{x}_2[k]+\boldsymbol{C}_{d2}\boldsymbol{B}_{d2}\boldsymbol{u}_2[k]+\boldsymbol{C}_{d2}\boldsymbol{D}_{d2}\\\qquad\Delta P=P_{set}^{hvdc}-\left(P_{wg}^{for}+P_{m,2}-P_{asl}-P_{nl,2}\right)\\\qquad\boldsymbol{u}_{2,\min}\le\boldsymbol{u}_2[k]\le\boldsymbol{u}_{2,\max}\\\qquad\boldsymbol{u}_2[k]-\boldsymbol{u}_2[k-1]\le\Delta\boldsymbol{u}_{2,\max}\\\qquad\boldsymbol{f}_{\min}+\boldsymbol{\Omega}_\beta\le\boldsymbol{y}_2[k+1]\le\boldsymbol{f}_{\max}-\boldsymbol{\Omega}_\beta\end{cases} \tag{59}$$

3) Determination of MPC Parameters

This subsection introduces a method for determining the control step T_{c2}, prediction horizon T_{p2}, and $\boldsymbol{Q}_{21}$ and $\boldsymbol{Q}_{22}$ of MPC controller 2 in the PPS system.

Similar to the MPC controller in the RPS system, the control step and prediction horizon of the MPC controller in the PPS system are also selected to be $T_{c2}=5$ s and $T_{p2}=10$ s, respectively.

Correspondingly, $\boldsymbol{Q}_{21}$ is kept constant, and $\boldsymbol{Q}_{22}$ is time-varying, which is determined by the feedback power deviation ΔP_2^{for}:

$$\boldsymbol{Q}_{22}=\boldsymbol{Q}_{22}^s-\boldsymbol{K}_{q2}\Delta P_2^{for} \tag{60}$$

where $\boldsymbol{Q}_{22}^s$ and $\boldsymbol{K}_{q2}$ are the standard value and droop coefficient of $\boldsymbol{Q}_{12}$, respectively.

C. Flowchart of Proposed Control Schemes

Flowcharts of the proposed control schemes of the RPS system and PPS system are shown in Fig. 4. In the two systems, the MPC controllers collect ACE signals in real time for SFC. In small disturbance scenarios, the control variable

of the RPS system is the set point of the AGC units, and it is the set point of the self-owned generators in the PPS system. However, if ACE_1 exceeds the preset threshold ACE_{trig} (heavy disturbance scenarios), EDCPS will be triggered. In the RPS system, the set points of the AGC units and the power injection of VSC1 will be taken as the control variables. Meanwhile, the calculated P_{set}^{hvdc} will be sent to the PPS system as a feed-forward signal. In the PPS system, if EDCPS is triggered, the ASLs will also participate in SFC. The integrated power of the VPP will be controlled to track the feed-forward signal, which aims to counteract the power imbalance caused by EDCPS. The SFC process of the RPS system and PPS system continues until the ACE signals are reduced to the required value ACE_{req}. If an ACE signal (ACE_1 or ACE_2) is below ACE_{req}, the control of the corresponding system will stop.

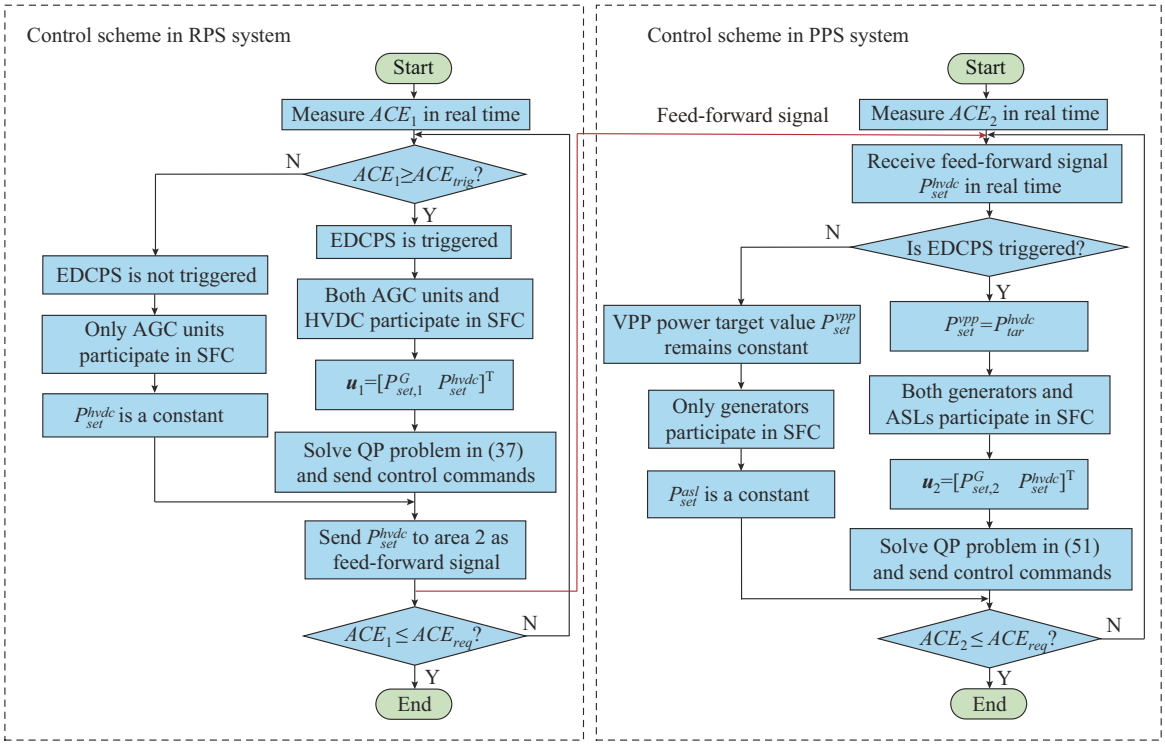

Fig. 4. Flowchart of proposed control scheme.

The control of the two systems operates independently. The end of control in one system does not affect the continuation of the control in the other system. If ACE_1 is below ACE_{req}, the control of the RPS system will be stopped, but the control of the PPS system can continue if $ACE_2 > ACE_{req}$. Accordingly, if ACE_2 is below ACE_{req}, the control of the PPS system will be stopped, and the control of the RPS system can continue if $ACE_1 > ACE_{req}$. When both ACE_1 and ACE_2 are controlled to be lower than ACE_{req}, the whole algorithm stops.

V. Case Study

In this section, simulation results are presented to demonstrate the effectiveness of the proposed MPC-based SFC strategy. The two-terminal HVDC power system shown in Fig. 5 is used as the test system. All simulations are performed using MATLAB. The optimizations invoke the Gurobi solver [35]. Given the long time scale of SFC, the detailed behaviors of the electronic power converters are ignored in the simulation.

The RPS system is modified from the New England 39-bus power system, where the generator in bus R39 is replaced by HVDC power injection from the PPS system. The total load power of the PPS system is 6196 MW, and detailed data of the New England 39-bus power system can be found in [36]. The PPS system is based on an actual industrial power grid in Inner Mongolia, China [24]. The industrial power grid consists of 15 buses. The generated power of G1-G4 is 350, 150, 540, and 600 MW, respectively. The normal load in bus P7 is 40 MW. The HVDC power exploration in bus P5 is 800 MW. The power consumed by ASL1-ASL3 is 350, 440, and 610 MW, respectively. The parameters of the VSC-HVDC system are listed in Table I. The data for ASL1-ASL3 are listed in Table II. We assume that wind farms WF1 and WF2 have the same wind speed, so they are simply considered to have the same power output. According to statistical data of the wind power output in [37], typical wind speed data and the probability distribution of the forecast error can be obtained, where the forecast error $e_{wg} \sim N(0, 0.036)$. Wind speed and total forecasted wind power of WF1 and WF2 are shown in Fig. 6. The initial value of the total wind power of WF1 and WF2 is rated at 600 MW.

Three cases are studied. In Case 1, the RPS system experiences a small disturbance with EDCPS, which is not triggered to demonstrate the effectiveness of the proposed MPC controller. In Case 2, two scenarios in which the RPS sys-

tem experiences a large disturbance (power shortage and power surplus) are considered to verify the effectiveness of EDCPS and ASL participation. In Case 3, the internal characteristics of the VSC-HVDC system and ASLs are presented.

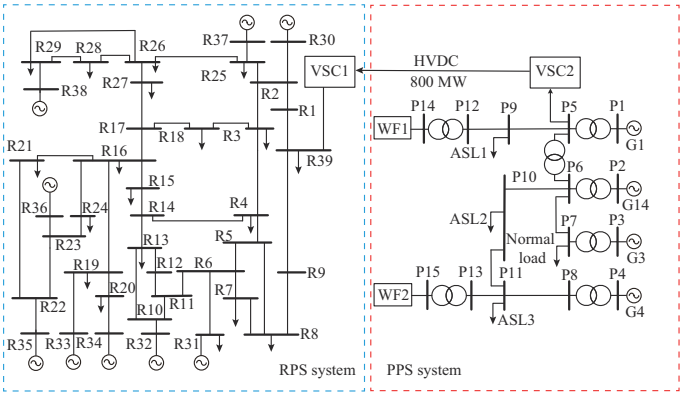

Fig. 5. Schematic diagram of test power system.

TABLE I
PARAMETERS OF VSC-HVDC SYSTEM

Description	Value	Description	Value
AC voltage of VSC1	220 kV	Line impedance	$0.1+j4\times10^{-4}$ Ω
AC voltage of VSC2	220 kV	Capacitor	1000 μF
DC voltage level	400 kV	Rated power	800 MW

TABLE II
DATA FOR ASL1-ASL3

Number	U_d (kV)	I_d (kA)	E_d (V)	R_d (mΩ)
ASL1	2.26	160.000	864	8.10
ASL2	1.54	624.000	576	2.88
ASL3	1.60	1.248	600	2.25

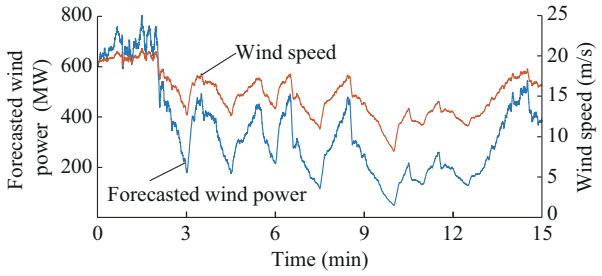

Fig. 6. Wind speed and total forecasted wind power of WF1 and WF2.

A. Case 1

This case is used to test the performance of the proposed MPC controllers with time-varying weight matrices. For comparison, traditional PI control, fuzzy PI control, and the fixed-weight MPC method are also evaluated in the same simulation environment. For the proposed varying-weight MPC method, $\boldsymbol{Q}_{11}$ and $\boldsymbol{Q}_{21}$ are diagonal matrixes consisting of 0.8. The standard values $\boldsymbol{Q}^s_{12}$ and $\boldsymbol{Q}^s_{22}$ are diagonal matrixes consisting of 0.2. For the fixed-weight MPC method, the weight matrixes are equal to the standard values of the corresponding parameters in the proposed MPC method. The parameters of traditional PI control are tuned by trial and error.

Firstly, the load power in bus R8 increases by 100 MW (about 1.6% of the total load power) at 100 s to create a power shortage in the RPS system. Then, the frequency of the RPS system drops because of the power shortage. The primary frequency control and secondary frequency control of the RPS system are triggered in succession. Since ACE_1 is small, EDCPS is not triggered, and only AGC units participate in frequency control.

The frequency curves of RPS system under different control methods are shown in Fig. 7. In the PFC period, the four methods have the same control performance because PFC is spontaneously carried out by the governor rather than the controller. In the SFC period, it is obvious that the proposed MPC method has better performance than that of the fixed-weight MPC method, and fuzzy PI control also has better performance than that of the traditional PI control. This is because the self-tuned characteristic of the varying-weight MPC and fuzzy PI controllers ensure that the parameters can be flexibly adjusted according to the signal error. However, even the fixed-weight MPC controller has superior performance to that of the fuzzy PI controller, which means that the MPC method can greatly reduce the period over which the frequency is restored in the RPS system.

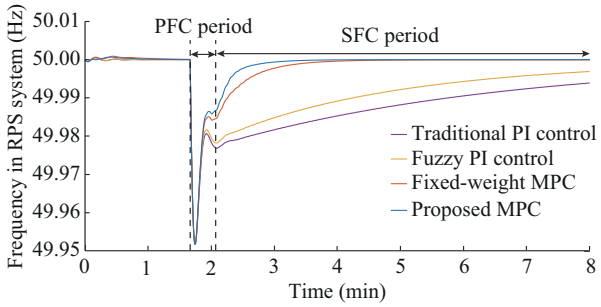

Fig. 7. Frequency curves of RPS system under different control methods.

In the PPS system, since EDCPS is not triggered, the power transmitted between the RPS system and the PPS system remains constant. The main disturbance in the PPS system comes from the fluctuation in the wind power. In the control process, ASLs maintain normal production, and only generators participate in VPP power control. As shown in Fig. 8(a), the target value of the VPP power output is kept constant (800 MW). For the two MPC methods, the VPP power output can be controlled near the target value even if the wind power greatly fluctuates. Further, the proposed MPC controller has better performance. By contrast, the performance of traditional PI control and fuzzy PI control is not good enough.

Frequency fluctuations in PPS system under different methods are shown in Fig. 8(b). The frequency for the proposed MPC method fluctuates less than that for other methods. This result corresponds to the control performance of the VPP power output. If the VPP power output is controlled near the target value, the power imbalance in the PPS sys-

tem can be reduced. Accordingly, the frequency devotion will be reduced. This means that the proposed MPC method can improve the wind power accommodation capacity of the PPS system. The peak values of deviations with different control methods are listed in Table III.

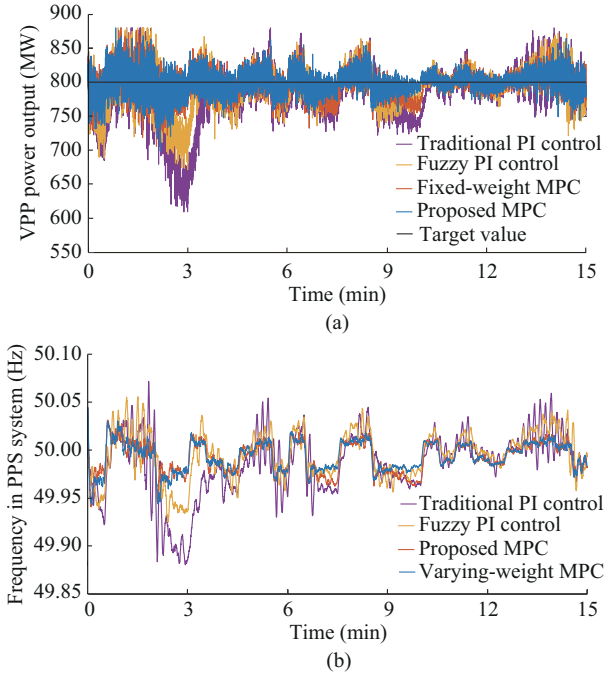

Fig. 8. Performance analysis. (a) VPP control performance with different control methods. (b) Frequency fluctuations in PPS system under different control methods.

TABLE III
PEAK VALUES OF DEVIATIONS WITH DIFFERENT CONTROL METHODS

Method	VPP deviation (MW)	Frequency deviation (Hz)
Traditional PI control	218.2485	0.1196
Fuzzy PI control	128.4429	0.0751
Fixed-weight MPC	101.5253	0.0592
Proposed MPC	94.0372	0.0564

B. Case 2

This case is used to verify the effectiveness of EDCPS and ASL participation in SFC when there is a large power shortage or power surplus in the RPS system. For comparison, the no-EDCPS scenario in the RPS system and the no-ASL scenario in the PPS system are evaluated in the same simulation environment. Fuzzy PI control is shown to have better performance than traditional PI control, so fuzzy PI control is used as a comparison for the proposed proposed MPC method.

In the power shortage scenario, a fault is set on bus R35 at 100 s, which causes a 650 MW power shortage (about 10.5% of the total load power) in the RPS system. In the power surplus scenario, the load power in bus R8 decreases by 500 MW (about 8% of the total load power) at 100 s. As a result, the frequency of the RPS system drops or rises sharply, and EDCPS is triggered. The HVDC transmission power rapidly increases or decreases to provide frequency control support.

The frequency control performance in RPS system with different control methods are shown in Fig. 9. From the results, the proposed MPC method has better performance than fuzzy PI control in both the EDCPS and no-EDCPS scenarios. Moreover, for the same control method, the participation of EDCPS can effectively shorten the frequency recovery time.

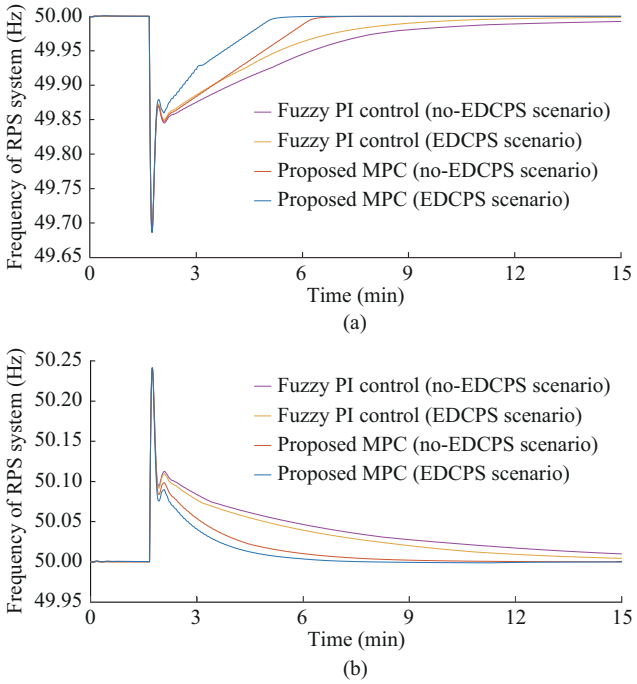

Fig. 9. Frequency control performance in RPS system with different control methods. (a) Power shortage scenario. (b) Power surplus scenario.

In the PPS system, the target value of the VPP varies with the feed-forward signal, as shown in Fig. 10. Then, the power output of the VPP is controlled to track the target value. The peak values of the power deviations of the VPP and the frequency deviations in the PPS system in different scenarios are listed in Table IV. From the results, the power output of the VPP with ASL participation using the proposed MPC method has the best performance than those of the other scenarios. Further, the performance of the two scenarios with ASL participation is better than that of the two no-ASL scenarios. This is because the flexibility of the ASL allows its participation to greatly improve the regulation ability of the VPP. Accordingly, the frequency fluctuations in Fig. 11 are related to the control performance of the VPP, where the proposed MPC method in the ASL scenario has the lowest frequency deviation, and fuzzy PI control in the no-ASL scenario has the highest frequency deviation.

C. Case 3

In this case, the effects of the proposed SFC strategy on the VSC-HVDC system and ASLs are discussed. The internal characteristics of the VSC-HVDC system and ASLs with the proposed MPC method in the power shortage and surplus scenarios mentioned in Case 2 are presented.

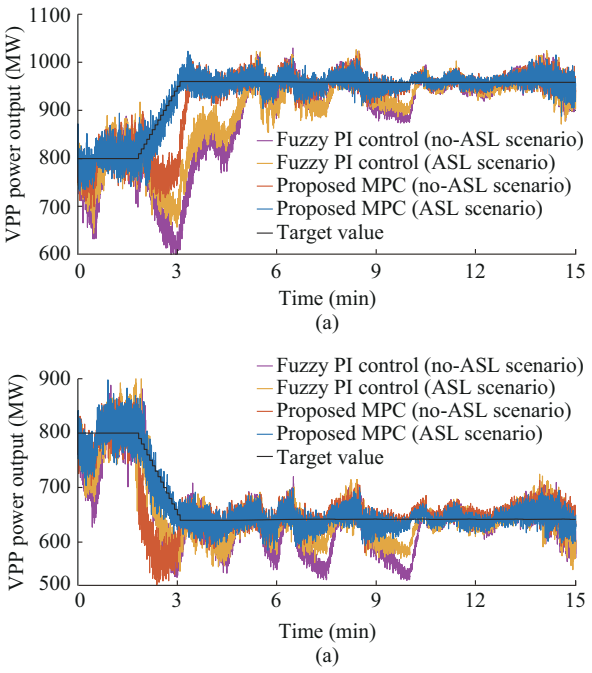

Fig. 10. VPP control performance with different control methods. (a) Power shortage scenario. (b) Power surplus scenario.

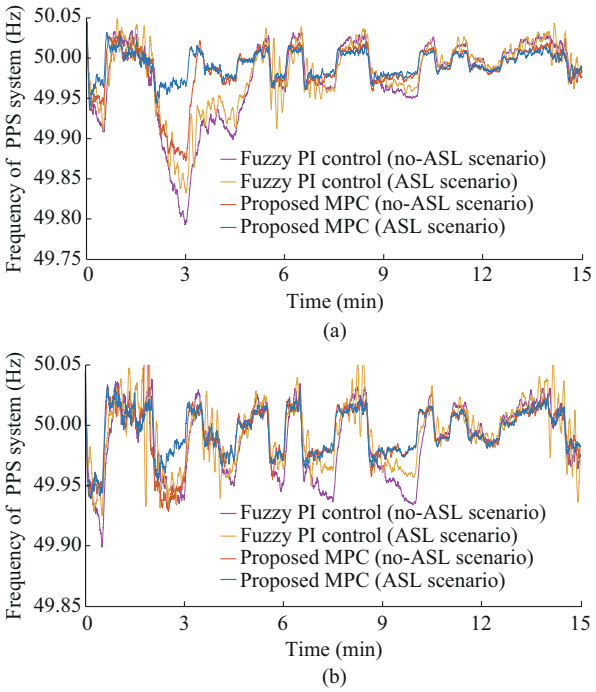

Fig. 11. Frequency fluctuations in PPS system with different control methods. (a) Power shortage scenario. (b) Power surplus scenario.

TABLE IV
PEAK VALUE OF DEVIATIONS IN DIFFERENT SCENARIOS

Scenario	VPP deviation (MW)		Frequency deviation (Hz)	
	ASL	No-ASL	ASL	No-ASL
Power shortage (proposed MPC)	94.3811	196.2015	0.0643	0.1280
Power shortage (fuzzy PI)	292.5823	358.2382	0.1677	0.2074
Power surplus (proposed MPC)	99.7494	118.0885	0.0608	0.0716
Power surplus (fuzzy PI)	133.2693	172.7302	0.0853	0.1010

The DC voltage of the VSC is an important index to evaluate the safe operation of the HVDC system. The variation of HVDC transmission power is shown in Fig. 12. The power injection of VSC2 is adjusted to follow the EDCPS command signal. Accordingly, the power injection in VSC1 is also changed due to DC voltage control. The variations in the DC voltages of VSC1 and VSC2 are shown in Fig. 13. During the transient process of EDCPS, the DC voltage increases or decreases because the active power injected into the inner DC system is not balanced. Then, as the transmission power stabilizes, the active power flowing into and out of the inner DC system quickly reaches a balance under the control of the VSC. Therefore, the DC voltages U_{dc1} and U_{dc2} are stabilized at new steady-state values. In the two scenarios, the peak value of the DC voltage deviation in the transient and steady-state processes are 17 kV (4.25%) and 0.61 kV (0.15%), respectively, which will not threaten the safe operation of the VSC-HVDC system.

As mentioned in [7], the electrolytic state of the ASLs is decided by I_d^{asl} in the potline.

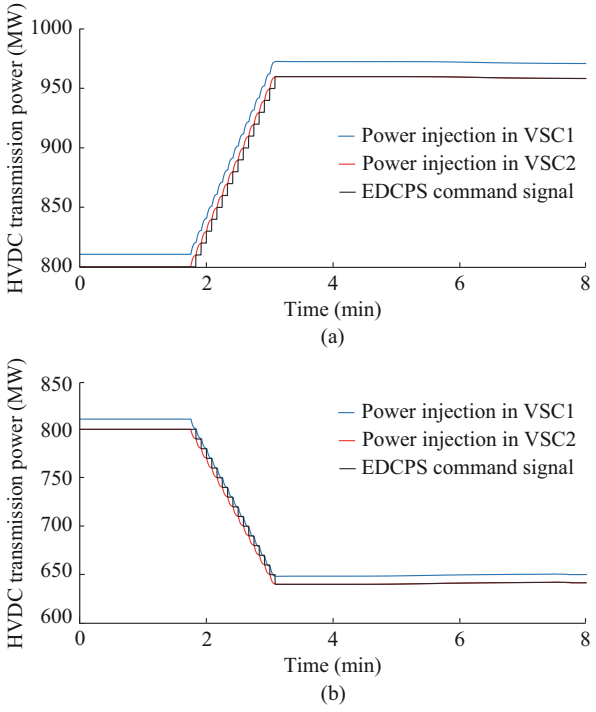

Fig. 12. Variation of HVDC transmission power. (a) Power shortage scenario. (b) Power surplus scenario.

The DC variations of ASL1 to ASL3 are shown in Fig. 14. During the control process, the ASLs adjust I_d^{asl} to change the power consumption. From the results, the DCs of the ASLs are always kept above 70% of the rated value, which is the security margin of aluminum electrolysis. Therefore, the safety of the ASLs can be guaranteed in the regulation process.

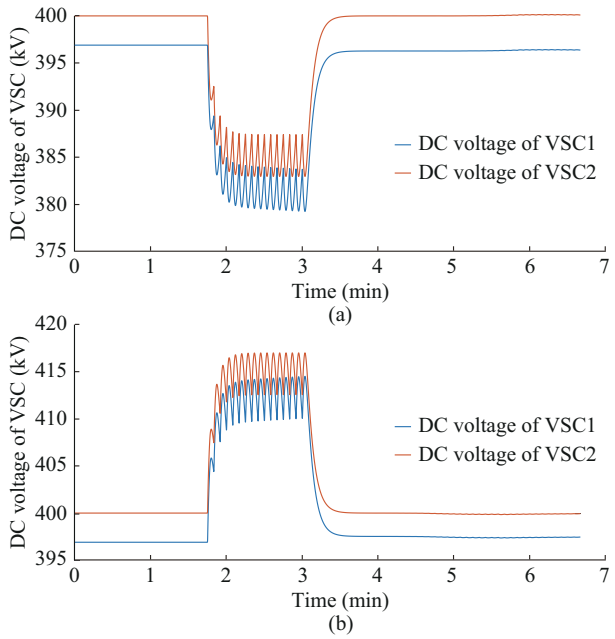

Fig. 13. DC voltages of VSC1 and VSC2. (a) Power shortage scenario. (b) Power surplus scenario.

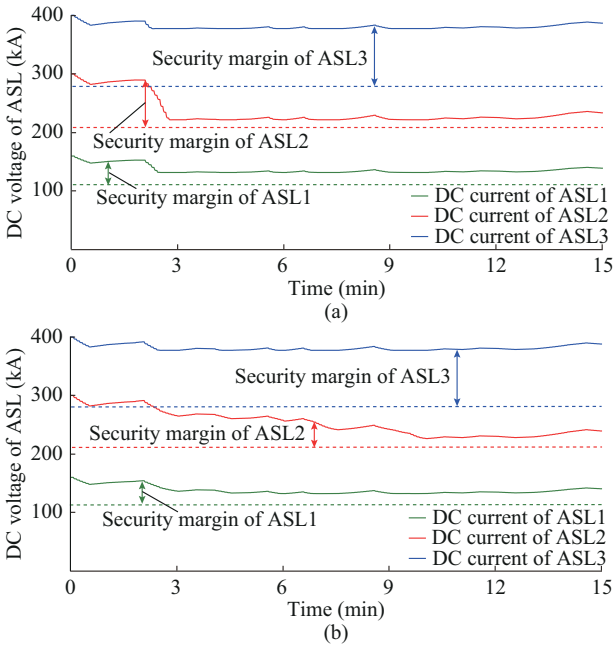

Fig. 14. DC variations of ASL1 to ASL3. (a) Power shortage scenario. (b) Power surplus scenario.

VI. Conclusion

We propose an SFC strategy involving EDCPS from an industrial power grid through a VSC-HVDC link. In the proposed strategy, two MPC controllers are set in the RPS system and PPS system with a distributed architecture. Time-varying weight matrices are adopted in the two MPC controllers to improve the transient performance. MPC controller 1 in the RPS system can shorten the frequency recovery time by obtaining the optimized EDCPS value. MPC controller 2 in the PPS system can reduce the adverse effects of EDCPS using a feed-forward signal in its prediction model. The industrial power grid serving as the PPS system is integrated as a VPP to obtain intuitive external characteristics. Simulations are performed using the data of an actual industrial power grid in Inner Mongolia, China. The following conclusions are drawn.

1) The EDCPS can alleviate the problem of a reserve shortage in the RPS system by sharing the reserves between the RPS system and the PPS system. Simulation results show that the participation of EDCPS can shorten the frequency recovery time of the RPS system in the large disturbance scenario.

2) The demand response of the ASLs improves the flexibility and controllability of the VPP model. Simulation results show that the control deviation of the power output of the VPP in the ASL scenario is much lower than that in the no-ASL scenario. Correspondingly, the undesired frequency oscillation caused by EDCPS is also reduced for the participation of the ASLs.

3) The proposed MPC controllers can improve the control performance of the RPS system and PPS system. A comparison with traditional PI control, fuzzy PI control, and fixed-weight MPC shows that the proposed MPC method with time-varying weight matrices has the best performance (the shortest frequency recovery time in the RPS system and the lowest frequency deviations in the PPS system).

4) The regulation of the VSC-HVDC and ASLs using the proposed control strategy will not cause a security problem. The DC deviations of the VSCs are small. The DCs in the potlines of the ASLs are also kept above the security margins.

References

[1] H. Li, N. Zhang, Y. Fan *et al.*, "Decomposed modeling of controllable and uncontrollable components in power systems with high penetration of renewable energies," *Journal of Modern Power Systems and Clean Energy*, vol. 10, no. 5, pp. 1164-1173, Sept. 2022.

[2] J. Frunt, "Analysis of balancing requirements in future sustainable and reliable power systems," Ph.D. dissertation, Department of Electric Engineering, Eindhoven University of Technology, Eindhoven, 2011.

[3] J. E. S. de Haan, J. Frunt, A. Kechroud *et al.*, "Supplementary control for wind power smoothing," in *Proceedings of 45th International Universities Power Engineering Conference*, Cardiff, Wales, Jan. 2010, pp. 1-5.

[4] M. Paulus and F. Borggrefe, "The potential of demand-side management in energy-intensive industries for electricity markets in Germany," *Applied Energy*, vol. 88, no. 2, pp. 432-441, Feb. 2011.

[5] H. Jiang, J. Lin, Y. Song *et al.*, "Demand side frequency control scheme in an isolated wind power system for industrial aluminum smelting production," *IEEE Transactions on Power Systems*, vol. 29, no. 2, pp. 844-853, Mar. 2014.

[6] H. Jiang, J. Lin, Y. Song *et al.*, "MPC-based frequency control with demand-side participation: a case study in an isolated wind-aluminum power system," *IEEE Transactions on Power Systems*, vol. 30, no. 6, pp. 3327-3337, Nov. 2015.

[7] P. Bao, W. Zhang, D. Cheng *et al.*, "Hierarchical control of aluminum smelter loads for primary frequency support considering control cost," *International Journal of Electrical Power & Energy Systems*, vol. 122, pp. 1-9, Nov. 2020.

[8] J. Renedo, A. García-Cerrada, and L. Rouco, "Active power control strategies for transient stability enhancement of AC/DC grids with VSC-HVDC multi-terminal systems," *IEEE Transactions on Power Systems*, vol. 31, no. 6, pp. 4595-4604, Nov. 2016.

[9] C. Guo, W. Liu, C. Zhao *et al.*, "A frequency-based synchronization approach for the VSC-HVDC station connected to a weak AC grid," *IEEE Transactions on Power Delivery*, vol. 32, no. 3, pp. 1460-1470, Jun. 2017.

[10] N. R. Chaudhuri, R. Majumder, and B. Chaudhuri, "System frequency support through multi-terminal DC (MTDC) grids," *IEEE Transactions on Power Systems*, vol. 28, no. 1, pp. 347-356, Feb. 2013.
[11] J. Fradley, R. Preece, and M. Barnes, "VSC-HVDC for frequency support (a review)," in *Proceedings of 13th IET International Conference on AC and DC Power Transmission (ACDC 2017)*, Manchester, UK, Feb. 2017, pp. 1-8.
[12] A. S. Elansari, S. J. Finney, J. Burr *et al*., "Frequency control capability of VSC-HVDC transmission system," in *Proceedings of 11th IET International Conference on AC&DC Power Transmission*, Beijing, China, Jul. 2015, pp. 1-7.
[13] C. Du, M. H. J. Bollen, E. Agneholm *et al*., "A new control strategy of a VSC-HVDC system for high-quality supply of industrial plants," *IEEE Transactions on Power Delivery*, vol. 22, no. 4, pp. 2386-2394, Oct. 2007.
[14] A. G. Endegnanew and K. Uhlen, "Global analysis of frequency stability and inertia in AC systems interconnected through an HVDC," in *Proceedings of IEEE International Energy Conference*, Leuven, Belgium, Apr. 2016, pp. 1-8.
[15] M. Yu, A. Dyśko, C. D. Booth *et al*., "A review of control methods for providing frequency response in VSC-HVDC transmission systems," in *Proceedings of 49th International Universities Power Energy Conference*, Cluj-Napoca, Romania, Sept. 2014, pp. 1-6.
[16] A. Junyent-Ferr, Y. Pipelzadeh, and T. C. Green, "Blending HVDC-link energy storage and offshore wind turbine inertia for fast frequency response," *IEEE Transactions on Sustainable Energy*, vol. 6, no. 3, pp. 1059-1066, Jul. 2015.
[17] S. D. Arco and J. A. Suul, "Virtual synchronous machines –classification of implementations and analysis of equivalence to droop controllers for microgrids," in *Proceedings of 2013 IEEE Grenoble Conference*, Grenoble, France, Jun. 2013, pp. 1-7.
[18] J. Driesen and K. Visscher, "Virtual synchronous generators," in *Proceedings of 2008 IEEE PES General Meeting*, Pennsylvania, USA, Jul. 2008, pp. 1-3.
[19] Q. Zhong and G. Weiss, "Synchronverters: inverters that mimic synchronous generators," *IEEE Transactions on Industrial Electronics*, vol. 58, no. 4, pp. 1259-1267, Apr. 2011.
[20] J. E. S. de Haan, C. E. Concha, M. Gibescu *et al*., "Stabilising system frequency using HVDC between the continental european, nordic, and great britain systems," *Sustainable Energy, Grids and Networks*, vol. 5, pp. 125-134, Mar. 2016.
[21] J. Dai, Y. Phulpin, A. Sarlette *et al*., "Coordinated primary frequency control among non-synchronous systems connected by a multi-terminal high-voltage direct current grid," *IET Generation, Transmission & Distribution*, vol. 6, no. 2, pp. 99-108, Feb. 2012.
[22] B. Silva, C. L. Moreira, L. Seca *et al*., "Provision of inertial and primary frequency control services using offshore multiterminal HVDC networks," *IEEE Transactions on Sustainable Energy*, vol. 3, no. 4, pp. 800-808, Oct. 2012.
[23] J. Dai, Y. Phulpin, A. Sarlette *et al*., "Impact of delays on a consensus-based primary frequency control scheme for AC systems connected by a multi-terminal HVDC grid," in *Proceedings of Bulk Power System Dynamics and Control Symposium*, Rio de Janeiro, Brazil, Aug. 2010, pp. 1-9.
[24] J. Lin, Y. Sun, Y. Songm *et al*., "Wind power fluctuation smoothing controller based on risk assessment of grid frequency deviation in an isolated system," *IEEE Transactions on Sustainable Energy*, vol. 4, no. 2, pp. 379-392, Apr. 2013.
[25] X. Chen, "Research on VSC-HVDC Active disturbance rejection control for improving power system stability," M.S. thesis, Department of Electric Engineering, South China University of Technology, Guangzhou, China, 2018.
[26] Z. Chao, X. Zhou, and R. Li, "Dynamic modeling and transient simulation for VSC based HVDC in multi-machine system," in *Proceedings of 2006 International Conference on Power System Technology,* Chongqing, China, Jun. 2006, pp. 1-7.
[27] C. Du and M. H. J. Bollen, "Power-frequency control for VSC-HVDC during island operation," in *Proceedings of 8th IEE International Conference on AC & DC Power Transmission*, London, UK, Jun. 2006, pp. 177-181.
[28] A. P. Agalgaonkar, K. M. Muttaqi, and S. Perera, "Response analysis of saturable reactors and tap changer in an aluminum smelting plant," in *Proceedings of 2009 International Conference on Power Systems*, Kharagpur, India, Jul. 2009, pp. 1-6.
[29] H. Xu, Q. Xu, Y. Gao *et al*., "Coordinate control strategy for current stabilization in an aluminum smelter including on load tap changer," *Energy & Power Engineering*, vol. 5. no. 4, pp. 1410-1414. Jul. 2013.
[30] J. L. Aguero, M. Beroqui, and S. Achilles, "Aluminum plant, load modeling for stability studies," in *Proceedings of 1999 IEEE PES Summer Meeting*, Edmonton, Canada, Aug. 1999, pp. 1330-1335.
[31] M. Negnevitsky, P. Johnson, and S. Santoso, "Short term wind power forecasting using hybrid intelligent systems," in *Proceedings of 2007 IEEE PES General Meeting*, Tampa, India, Feb. 2007, pp. 1-4.
[32] C. Wang, F. Liu, J. Wang *et al*., "Robust risk-constrained unit commitment with large-scale wind generation: an adjustable uncertainty set approach," *IEEE Transactions on Power Systems*, vol. 32, no. 1, pp. 723-733, Jan. 2017.
[33] M. Farina, L. Giulioni, and R. Scattolini. "Stochastic linear model predictive control with chance constraints – a review," *Journal of Process Control*, vol. 44, pp. 53-67, Jul. 2016.
[34] J. Paulson, E. Buehler, R. Braatz *et al*., "Stochastic model predictive control with joint chance constraints," *International Journal of Control*, vol. 93, no. 1, pp. 126-139, Jul. 2020.
[35] Curobi. (2021, Jan.). Gurobi Optimizer Reference Manual. [Online]. Available: https://www. gurobi. com/documentation/9.1/refman/index. html
[36] T. Athay, R. Podmore, and S. Virmani, "A practical method for the direct analysis of transient stability," *IEEE Transactions on Power Apparatus and Systems*, vol. 98, no. 2, pp. 573-584, Mar. 1979.
[37] B. Hodge and M. Milligan, "Wind power forecasting error distributions over multiple timescales," in *Proceedings of 2011 IEEE PES General Meeting*, Detroit, USA, Aug. 2011, pp. 1-8.

Peng Bao received the B. E. degree in electrical engineering from Zhengzhou University, Zhengzhou, China, in 2018 and the M.Sc. degree in electrical engineering from Shandong University, Jinan, China, in 2021. He is currently pursuing the Ph.D. degree in electrical engineering at Southeast University, Nanjing, China. His research interests include frequency control of power systems and demand response from aluminum smelter loads.

Wen Zhang received the B.S., M.S., and Ph.D. degrees from Shandong University, Jinan, China, in 1989, 1992, and 2006, respectively, all in electrical engineering. She is currently a Professor with the Key Laboratory of Power System Intelligent Dispatch and Control of Ministry of Education, Shandong University. Her current research interests include power system analysis and control, demand-side response, and application of artificial intelligence to power systems.

Yuxi Zhang received the B.E. degree in electrical engineering from Shandong University, Jinan, China, in 2020. She is currently pursuing the M.Sc. degree in Shandong University. Her research interests include power system analysis and control, and demand-side response.